



## ARTICLE OPEN



# Electron-beam-irradiated rhenium disulfide memristors with low variability for neuromorphic computing

Sifan Li<sup>1,2,3</sup>, Bochang Li<sup>1,2,3</sup>, Xuewei Feng<sup>1,2</sup>, Li Chen<sup>1,2</sup>, Yesheng Li<sup>1,2</sup>, Li Huang<sup>1,2</sup> , Xuanyao Fong<sup>1,2</sup>  and Kah-Wee Ang<sup>1,2</sup> 

State-of-the-art memristors are mostly formed by vertical metal–insulator–metal (MIM) structure, which rely on the formation of conductive filaments for resistive switching (RS). However, owing to the stochastic formation of filament, the set/reset voltage of vertical MIM memristors is difficult to control, which results in poor temporal and spatial switching uniformity. Here, a two-terminal lateral memristor based on electron-beam-irradiated rhenium disulfide ( $\text{ReS}_2$ ) is realized, which unveils a resistive switching mechanism based on Schottky barrier height (SBH) modulation. The devices exhibit a forming-free, stable gradual RS characteristic, and simultaneously achieve a small transition voltage variation during positive and negative sweeps (6.3%/5.3%). The RS is attributed to the motion of sulfur vacancies induced by voltage bias in the device, which modulates the  $\text{ReS}_2$ /metal SBH. The gradual SBH modulation stabilizes the temporal variation in contrast to the abrupt RS in MIM-based memristors. Moreover, the emulation of long-term synaptic plasticity of biological synapses is demonstrated using the device, manifesting its potential as artificial synapse for energy-efficient neuromorphic computing applications.

npj 2D Materials and Applications (2021)5:1; <https://doi.org/10.1038/s41699-020-00190-0>

## INTRODUCTION

Memristors have been investigated extensively and are regarded as one of the artificial synapse candidates for neuromorphic computing<sup>1–6</sup>. Among these memristors, the switching mechanisms are primarily relying on the formation of conductive filaments in the insulating layers, such as the valence change mechanism (VCM) and electrochemical metallization (ECM)<sup>7</sup>. For VCM-based devices, the conductance change is induced by the migration of vacancy anions, such as oxygen vacancies<sup>8–11</sup>. However, due to the random distribution of vacancy anions in the insulator, the formation of anion filament is a stochastic process<sup>7,12,13</sup>. The resistive switching (RS) of ECM devices is caused by the motion and metallization of active electrode metal cations, such as  $\text{Ag}^+$  (refs. 14–16). However, such highly mobile metal cations are difficult to control during the electroforming steps due to the stochasticity of the migration path of these cations<sup>7,13,17</sup>. As such, for both VCM- and ECM-based devices, the temporal (cycle-to-cycle) variation is inevitable because of the random formation and rupture of the conductive filaments. To overcome this issue, Choi et al. demonstrated an epitaxial random access memory (ePiRAM) based on single-crystalline  $\text{SiGe}$ <sup>18</sup>. The ePiRAM achieved a small set voltage variation due to the confinement of Ag filaments, and accurate control of dislocation density. However, the device still cannot avoid temporal variation during the eradication of the filament. Thus, the search for a non-filamentary switching mechanism is essential to control the cycle-to-cycle variation. In addition, the high molecular beam epitaxy (MBE) growth temperature is not suitable for the integration of such ePiRAM with complementary metal oxide semiconductor (CMOS) technology<sup>14</sup>. In terms of back-end-of-line (BEOL) compatibility, two-dimensional (2D) materials emerge as alternative choices due to the development of low-temperature 2D material growth by chemical vapor deposition (CVD) and large-scale 2D material transfer technology<sup>19–23</sup>.

Many vertical memristors based on 2D materials and their derivatives have been demonstrated. Some of these switching layers are made of pure 2D materials (e.g.  $\text{MoS}_2$ , hBN,  $\text{WSe}_2$ ) and the switching mechanisms are based on native defects in the materials (e.g. sulfur vacancies and boron vacancies) and the formation of active metal filament (e.g. Ag, Ti and Cu)<sup>24–27</sup>. Both short-term and long-term synaptic plasticity have been emulated in these devices<sup>24,25</sup>. Moreover, vertical memristors based on 2D-material derivatives (e.g.  $\text{MoO}_x/\text{MoS}_2$ ,  $\text{WO}_x/\text{WSe}_2$ ) are reported with low switching voltage due to the thin oxidation layer thickness<sup>28,29</sup>. Such vertical memristors are suitable for device scaling to enable high-density array integration<sup>30,31</sup>. In addition, compared to lateral memristors, vertical memristors show smaller set voltage due to a thinner switching layer<sup>2,15,28</sup>. However, their two-terminal structure is not suitable for multi-terminal bio-synapse emulation. Compared to vertical memristors, lateral memristors are more versatile to realize multi-terminal memristor by adding more electrodes<sup>32,33</sup>. Recently,  $\text{MoS}_2$ -based lateral memristive devices are reported, which relied on voltage-bias-induced sulfur vacancy motion and Schottky barrier height (SBH) modulation at the metal/ $\text{MoS}_2$  contact regions<sup>32,34,35</sup>. Such switching scheme distinguishes these memristors from filamentary memristors and may reduce the variation caused by the stochastic filament formation process. Moreover, the search for new materials which are easier to create sulfur vacancies may improve the switching performance. Rhenium disulfide ( $\text{ReS}_2$ ), a type of 2D material with weak interlayer coupling, soft Re–S covalent bonds, and low sulfur vacancy forming energy, may experience more obvious sulfur vacancy motion when subjected to external bias<sup>36–38</sup>.

Here, we start from single-crystalline 2D  $\text{ReS}_2$  and demonstrate a  $\text{ReS}_2$ -based lateral memristor by introducing sulfur vacancies into the material. The device exhibits forming-free gradual RS characteristic. A small cycle-to-cycle variation of transition voltage

<sup>1</sup>Department of Electrical and Computer Engineering, National University of Singapore, 4 Engineering Drive 3, Singapore 117583, Singapore. <sup>2</sup>Center for Advanced 2D materials, National University of Singapore, 6 Science Drive 2, Singapore 117546, Singapore. <sup>3</sup>These authors contributed equally: Sifan Li, Bochang Li. ✉email: [kelvin.xy.fong@nus.edu.sg](mailto:kelvin.xy.fong@nus.edu.sg); [eleakw@nus.edu.sg](mailto:eleakw@nus.edu.sg)

during positive and negative sweeps is achieved (6.3% and 5.3%). As opposed to filamentary switching mechanism, the RS is originating from voltage-bias-induced motion of sulfur vacancies in  $\text{ReS}_2$ , which modulates the metal/ $\text{ReS}_2$  SBH. The resulting gradual RS enables a small variation in direct current (DC) sweeps as compared to the abrupt switching in filament-based memristors. In this  $\text{ReS}_2$  memristor, we confirm the feasibility of the electron beam irradiation (EBI) in introducing defects into  $\text{ReS}_2$  by transmission electron microscopy (TEM). To further investigate the effect of EBI on  $\text{ReS}_2$ , detail material studies are carried out. A rectification-mediated switching characteristic is identified, which is different from typical non-volatile memristors and requires a fixed reading voltage polarity<sup>32</sup>. Moreover, the RS mechanism is analyzed based on selective EBI between the contact and  $\text{ReS}_2$  active regions and temperature-dependent current-voltage measurements. The influence of electron beam dosage and flake thickness on RS ratio are also discussed. Finally, the device is used as an artificial synapse, which enables the emulation of long-term potentiation (LTP), long-term depression (LTD), paired pulse facilitation (PPF), paired pulse depression (PPD), spike-amplitude-dependent plasticity (SADP), and spike-timing-dependent plasticity (STDP).

## RESULTS

### Characterization of electron-beam-irradiated $\text{ReS}_2$

As shown in Fig. 1, we have fabricated a two-terminal planar  $\text{ReS}_2$ -based memristor device. Figure 1a shows a structural schematic of the as-fabricated  $\text{ReS}_2$  memristor. The device is designed with lateral configuration, and the flake is selectively irradiated by focused electron beam, as shown in Fig. 1b. The guidelines inside  $\text{ReS}_2$  indicate the defects created by EBI. The composition of the defects will be discussed in detail later. A scanning electron microscope (SEM) image of four  $\text{ReS}_2$  memristors fabricated on the same flake is shown in Fig. 1c. There are eight parallel electrodes from left to right and each pair of electrodes form a lateral memristor. The EBI dosages of these devices from left to right are 8000, 6000, 4000, and 0  $\mu\text{C cm}^{-2}$  (pristine flake), respectively.

Next, we investigate the properties of electron-beam-irradiated  $\text{ReS}_2$  by performing TEM analysis on the same flake to verify the feasibility of EBI in creating defects in  $\text{ReS}_2$  flakes. Figure 1d shows a TEM image at the contact region with EBI dosage of 6000  $\mu\text{C cm}^{-2}$ . The thickness of the flake is 3 nm, which consists of five-layer  $\text{ReS}_2$  with each monolayer having a thickness of 0.6 nm<sup>39</sup>. The insets show obvious contrast between lattice disorders (labeled by red outline) and layer-by-layer structure (labeled by green outline). The image of lattice structure becomes blurry when it is distorted by lattice disorders<sup>25,35</sup>. Since EBI is carried out before metal deposition (see "Methods"), both the contact and the  $\text{ReS}_2$  active regions in Fig. 1c are irradiated. Lattice disorder in  $\text{ReS}_2$  active region is also found (as shown in Fig. 1e). Additional TEM analysis of other highlighted regions in Fig. 1c with different dosages is described in Supplementary Figs. 1–4, and lattice disorders are also found in the  $\text{ReS}_2$  flake. It is interesting to note that lattice disorders are found in all contact edges (see Fig. 1f and Supplementary Fig. 3), which may be related to the effect of electrical measurement and will be discussed in device characterization section. Based on these images, we postulate that EBI with appropriate dosage (4000–8000  $\mu\text{C cm}^{-2}$ ) can create defects in  $\text{ReS}_2$  flake. The non-uniform distribution of defects in the TEM images may be attributed to the difference in forming energy among the defects at different sites in  $\text{ReS}_2$  (ref. 38). Further top-view TEM characterizations would shed light on the spatial distribution of the lattice disorders<sup>40</sup>.

Apart from TEM, material analysis is also performed to understand the impact of EBI dosage on the density of defects, and the mechanism of defects formation in  $\text{ReS}_2$ . First, dosage

dependence of defect density is investigated through topographical and optical analysis. Figure 2a shows the atomic force microscopy (AFM) phase images of  $\text{ReS}_2$  flakes that are irradiated with different dosages. Pristine flake is shown to exhibit a uniform surface with little wrinkles which may be caused by mechanical exfoliation<sup>41</sup>. When EBI dosage is increased, the flake surface becomes rough and some crack-like features are formed. The density of such feature increases with EBI dosage. Such phenomenon indicates that more defects may be created in  $\text{ReS}_2$  flakes when exposed to higher EBI dosage. In addition to topographical analysis by AFM, Raman and Photoluminescence (PL) analysis are also performed to further confirm the formation of defects, which may be more sensitive to the existence and density of defects as compared to AFM. This is because the lattice vibration mode and radiative recombination process in material are highly dependent on the crystal structure and defect density. Figure 2b shows the Raman spectra of flake between 125 and 225  $\text{cm}^{-1}$  under different EBI dosages. Since  $\text{ReS}_2$  is an anisotropic material, the Raman spectra are recorded at the same flake orientation ([010]) to eliminate crystal orientation influence<sup>42</sup>. The two labeled peaks correspond to in-plane ( $E_g$ ), and out-of-plane ( $A_g$ ) vibration modes of  $\text{ReS}_2$ , respectively<sup>37,42,43</sup>. The full range of Raman spectra can be found in Supplementary Fig. 5. The irradiated flake shows a blue-shift phenomenon of both  $E_g$  and  $A_g$  peaks of about 1.26  $\text{cm}^{-1}$  (see Supplementary Fig. 5) in  $\text{ReS}_2$  with EBI dosage from 0 to 8000  $\mu\text{C cm}^{-2}$ . Such blue-shift of Raman peaks is caused by the relaxation of atom-atom vibration in 2D structure, indicating that more defects are created in  $\text{ReS}_2$  when exposed to larger dosage<sup>43</sup>.

Furthermore, PL spectra scans on the same flake are shown in Fig. 2c. Pristine  $\text{ReS}_2$  shows a broad signal located at about 1.52 eV, which is consistent with previous PL study<sup>36</sup>. After EBI, the PL signal becomes broader and the intensity decreases. Although there is little difference in PL intensity with different EBI dosages, it is still evident that EBI can form defects in  $\text{ReS}_2$ , which may lead to more nonradiative recombination process that reduces the PL intensity<sup>38</sup>. Based on all these characterizations, it is confirmed that EBI can engineer defects in  $\text{ReS}_2$  flakes, in which higher dosage increases the defect density. The chemical composition of the defects is also clarified. According to theoretical calculation results, sulfur vacancies have the lowest forming energy in  $\text{ReS}_2$  (ref. 38). Compared with other transient metal dichalcogenides (TMDs), sulfur vacancies in  $\text{ReS}_2$  are easier to form due to the relatively soft Re-S covalent bonds and weak interlayer coupling<sup>36,38</sup>. In addition, previous studies of  $\text{ReS}_2$  defects engineering using electron beam, oxygen plasma, and helium ions show that sulfur vacancies were the most common defects to be created inside the flakes<sup>37,38,40</sup>. X-ray photoelectron spectroscopy (XPS) is carried out to test our hypothesis. Figure 2d and e shows the XPS spectra of Re 4f and S 2p before and after EBI with a dosage of 6000  $\mu\text{C cm}^{-2}$ . The peak at 162.4 eV may originate from the contamination of polydimethylsiloxane (PDMS) during sample preparation as shown in Supplementary Fig. 6. After EBI, binding energies of both Re 4f and S 2p are shifted to a smaller value. The specific binding energies and shift values are shown in Supplementary Table 1. Such binding energy shift further proves that defects are created in  $\text{ReS}_2$  flakes after EBI, which is consistent with the binding energy shift reported in defective  $\text{MoS}_2$  (ref. 44). In addition, the atomic ratio of S atoms to Re atoms is extracted in  $\text{ReS}_2$  before and after irradiation. The extracted atomic ratio of S/Re is 1.99 and 1.87 in as-exfoliated flakes and irradiated flakes, respectively. The reduction of atomic ratio proves the formation of sulfur vacancies in  $\text{ReS}_2$ . Based on the EBI dosage and defect composition analysis, Fig. 2f shows a schematic illustration of how electron beam introduces sulfur vacancies in  $\text{ReS}_2$ , wherein the highlighted circles indicate the presence of sulfur vacancies due to the sputtering effect of electron beam. Intuitively, larger EBI

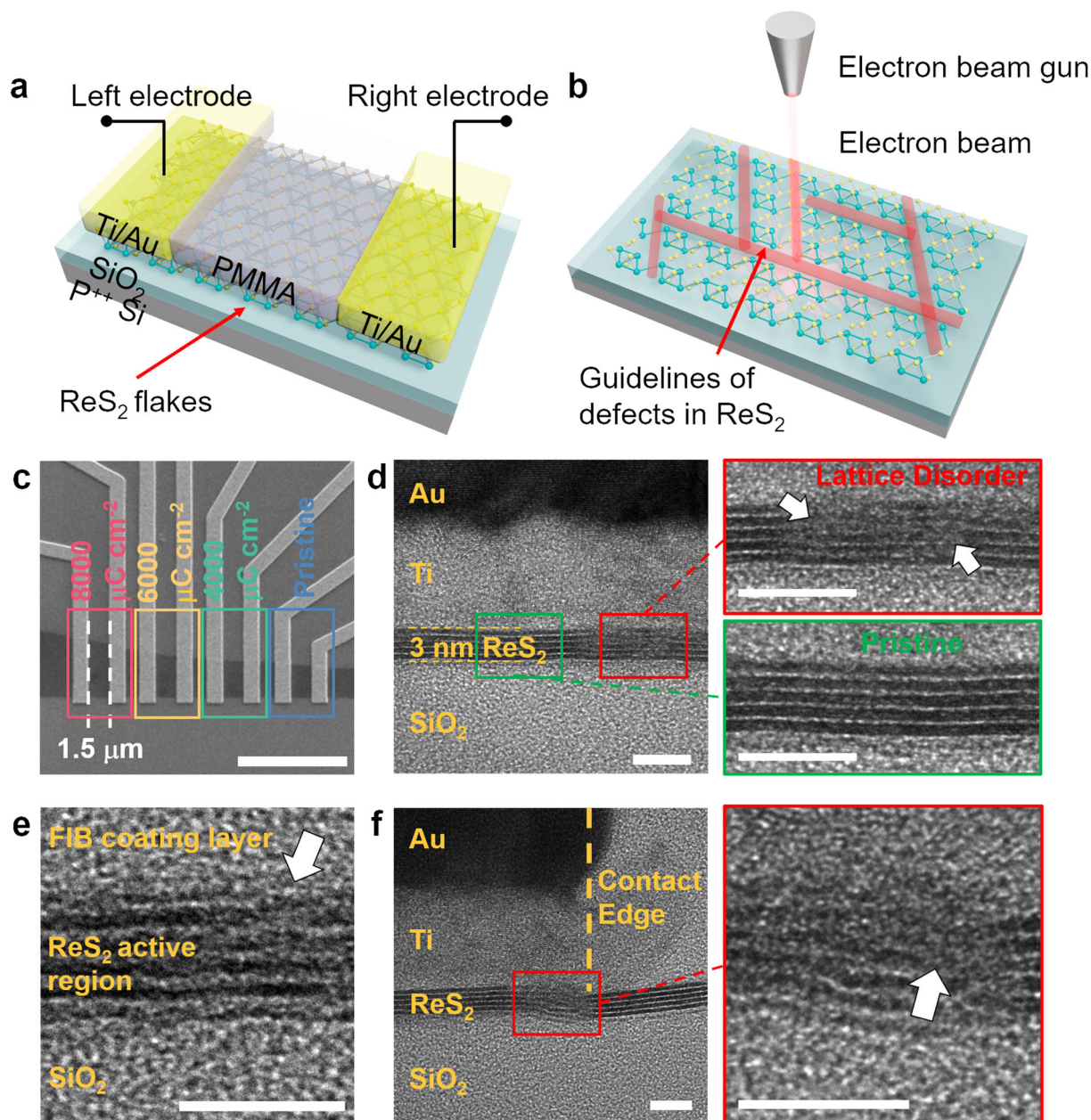


**Fig. 1** **Structure of ReS<sub>2</sub> memristor.** **a** A structural schematic of our ReS<sub>2</sub> planar memristor. **b** A schematic illustration of EBI. Selective area irradiation was performed by focused electron beam. The red lines in ReS<sub>2</sub> show the guidelines of defects. **c** SEM image of ReS<sub>2</sub> memristors. The distance between two electrodes is 1.5 μm. The highlighted squares show the irradiation dosage and regions. Scale bar, 5 μm. **d–f** Cross-section TEM images of a ReS<sub>2</sub> memristor under 6000 μC cm<sup>-2</sup> EBI. **d** At contact region. Insets show zoom-in images of lattice disorder (red) and pristine crystal structure (green). The white arrows show position of lattice disorders. Scale bar, 5 nm. **e** At ReS<sub>2</sub> active region. Scale bar, 5 nm. **f** At contact edge. The yellow dashed line labels the contact edge position. Inset shows the zoom-in image of lattice disorders (red). Scale bar, 5 nm.

dosage leads to more electrons bombarding the flake, which causes higher sulfur vacancies density.

#### Characteristics of ReS<sub>2</sub>-based memristor device

A schematic of the current–voltage (*I*–*V*) curve of such ReS<sub>2</sub>-based memristors is shown in Fig. 3a. The black dashed line refers to the full loop of current during voltage sweep. The black arrows labeled with numbers indicate the voltage sweep order during measurement. It should be noted that the RS characteristics, termed as rectification-mediated switching characteristics<sup>32</sup>, are different from the typical *I*–*V* curves of non-volatile memory. In typical non-volatile characteristics, current increases under one

voltage polarity (e.g. positive bias) and decreases with the opposite voltage polarity (e.g. negative bias)<sup>34</sup>. Different from that, the measured current in ReS<sub>2</sub>-based memristors switches from low current to high current under both positive and negative bias.

According to the previous MoS<sub>2</sub> work, such gradual RS behaviors may be related to the sulfur vacancies motion as induced by voltage bias effect, which modulates the SBH at the contact regions<sup>32,34</sup>. Positively charged sulfur vacancies in MoS<sub>2</sub> have been reported<sup>32</sup>, where RS curve switches from high current to low current under both positive and negative biases. Sulfur vacancies in ReS<sub>2</sub> are, however, negatively charged as these



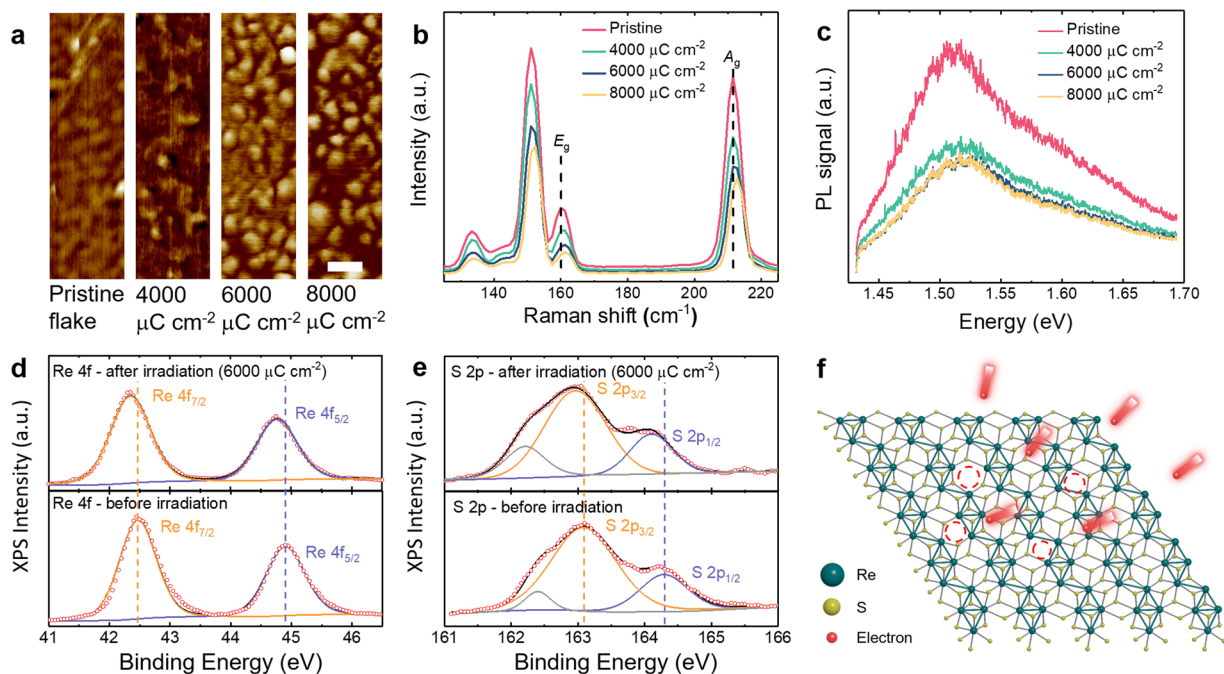


**Fig. 2** **Characterization of electron-beam-irradiated ReS<sub>2</sub>.** **a** AFM phase images taken with different EBI dosages. Scale bar, 50 nm. **b** Raman spectra of ReS<sub>2</sub> with different EBI dosages. The dashed lines label the blue shift of E<sub>g</sub> and A<sub>g</sub> peaks. **c** PL spectra of ReS<sub>2</sub> flake with different dosages. **d, e** XPS signal of Re 4f and S 2p peaks before and after EBI with a dosage of 6000 μC cm<sup>-2</sup>, respectively. The dashed lines label the peak position shift in XPS signal. **f** A schematic illustration of as-created sulfur vacancies during EBI.

vacancies have also been reported to serve as mobile species in MoS<sub>2</sub>-based memristive devices<sup>45–47</sup>. During the measurement, right electrode is always grounded, and a voltage is applied on left electrode. The red curve and blue curve in Fig. 3a are defined as forward-diode (FD) state and backward-diode (BD) state, respectively<sup>32</sup>. Figure 3b and c shows the measured data for FD state and BD state under different voltage sweep ranges. The full range *I*–*V* curves will be discussed later (see Fig. 4e). Here, a larger voltage sweep range leads to a larger rectification degree for both FD and BD states, indicating that a more effective SBH modulation is achieved under stronger electric field. The difference in current between FD and BD state may be attributed to the variation and distribution of sulfur vacancies induced by EBI. Similar minor asymmetric characteristics are also found in MoS<sub>2</sub>-based devices<sup>32</sup>. In-depth investigation should be carried out to unveil the fundamental reason. As shown in Fig. 3d–g, the detail mechanism of SBH modulation and sulfur vacancies motion are described using energy band diagrams and qualitative device models. During the positive voltage sweep (processes 1 and 2 in Fig. 3a), the negatively charged sulfur vacancies are drifted from right to left contact (see band diagram in Fig. 3d). This causes a decrease (increase) in sulfur vacancy density at right (left) contact, which alleviates (enhances) the Fermi level pinning (FLP) effect and results in a lower SBH at right contact and a high SBH at left contact. The modulation of SBH after positive voltage sweep is labeled by red dashed line in the band diagram (see Fig. 3d). The device can be regarded as two back-to-back connected Schottky diodes with a series resistance in the middle (as shown in Fig. 3e and g). After the device is stressed with positive voltage sweep, SBH at the right contact is less than SBH at the left contact. Such asymmetric back-to-back connected Schottky diodes result in *I*–*V* curve as shown in Fig. 3e, which is similar to a single Schottky diode under forward bias<sup>48</sup>. After this positive voltage sweep, it is termed as FD state. Next, during the transition of 3 and 4 in Fig. 3a, sulfur vacancies are drifted away from left to right electrode, which enhances (alleviates) the FLP effect and results in a high SBH at right contact and a low SBH at left contact (see Fig. 3f).

The change of SBH after negative voltage sweep is labeled by the blue dashed line in the band diagram (see Fig. 3f). This gives rise to an expected *I*–*V* curve as shown in Fig. 3g, which resembles a backward biased single Schottky diode. After such a negative voltage sweep, it is termed as BD state. Retention test shows that such FD state and BD state can be retained for longer than 700 s without external bias (see Supplementary Fig. 7 for details). Although the retention time is longer than volatile memristors<sup>2</sup>, compared to memristors with typical non-volatile characteristics by Sangwan et al., the retention time of our devices is shorter than 1500 min<sup>34</sup>. The short retention time of our device may indicate that sulfur vacancies are very mobile with a low diffusion barrier, which is attributed to the low forming energy of sulfur vacancies in ReS<sub>2</sub><sup>38</sup>. In addition, such gradual decrease in retention curves is consistent with the results reported in other lateral memristors, in which the explanation is also based on sulfur vacancy diffusion<sup>45</sup>.

To verify this mechanism, we first consider the possibility of voltage-bias-induced sulfur vacancy motion in ReS<sub>2</sub>. Electric field which can drift sulfur vacancies in polycrystalline MoS<sub>2</sub> and helium-ion-irradiated MoS<sub>2</sub> is typically larger than 10<sup>4</sup> V cm<sup>-1</sup> (refs. 32,34,45). In this work, the electric field is around 30,000 V cm<sup>-1</sup>, which is comparable to the minimum activation field. In addition, due to the relatively soft covalent bonds in ReS<sub>2</sub>, the motion of sulfur vacancies in ReS<sub>2</sub> may need a smaller electric field in contrast to that in MoS<sub>2</sub><sup>38</sup>. Next, we prove that such RS is caused by sulfur vacancies at contact regions by performing selective EBI on control samples. It is shown that only devices irradiated at contact regions or both contact and ReS<sub>2</sub> active regions exhibit obvious RS behaviors (see Supplementary Fig. 8), indicating that such RS behaviors are predominantly originated from sulfur vacancies at the contacts, wherein vacancies in the ReS<sub>2</sub> active region facilitate the movement of vacancies to the contact regions. Then, the movement of sulfur vacancies as induced by voltage bias is supported by Fig. 1f and Supplementary Fig. 3. Since EBI is performed before electrode patterning, there is equal probability to create defects in every region of the flake. However, it is shown that defects are found in all contact edges, which

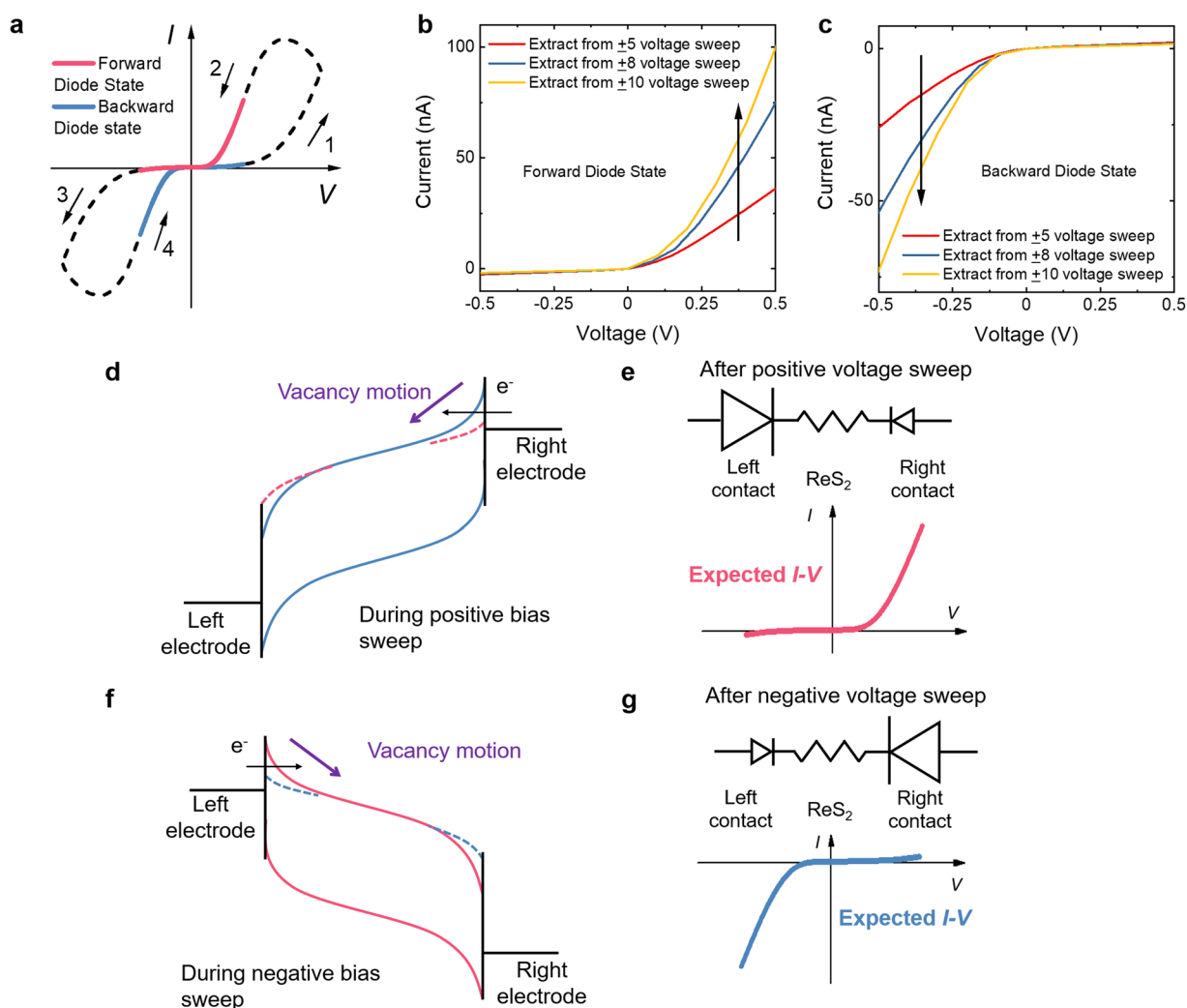
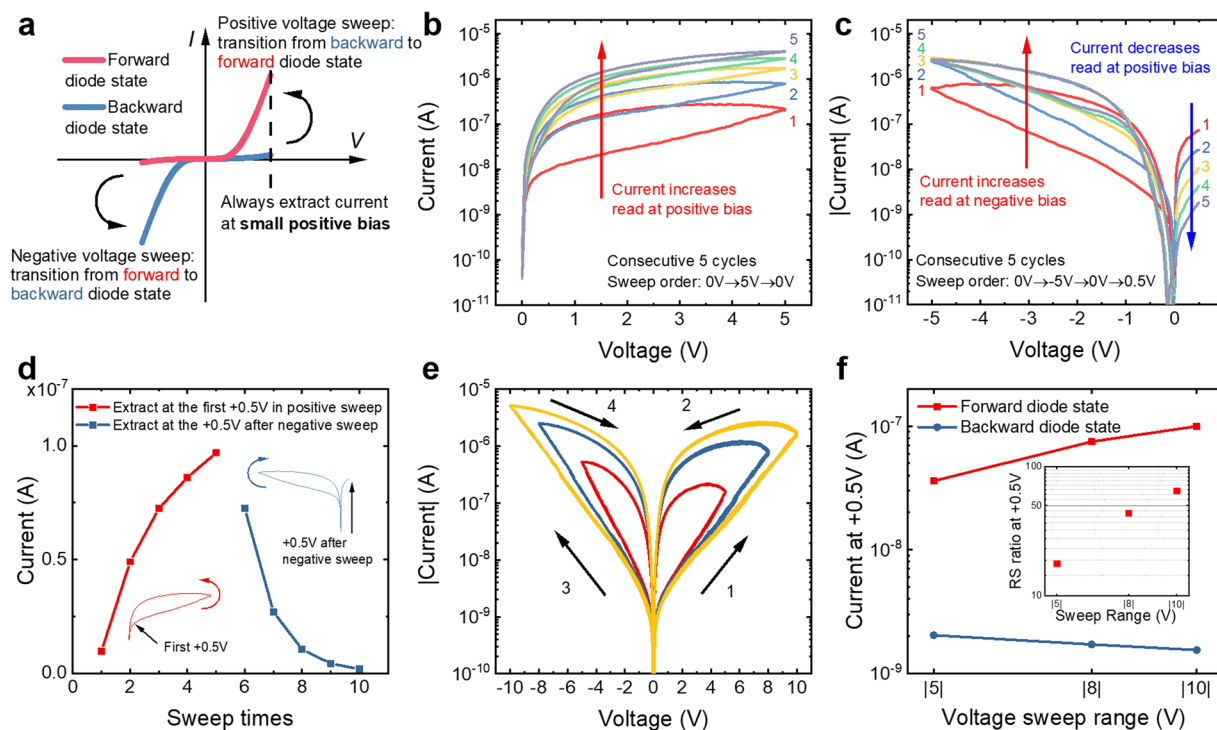


**Fig. 3** Operation mechanism of  $\text{ReS}_2$  memristors. **a** Schematic of  $I$ - $V$  curve in linear scale. The black arrows indicate the voltage sweep order. The red and blue curves are two states at small voltage range after positive and negative voltage sweeps, respectively. **b**, **c** Forward and backward-diode state  $I$ - $V$  curves extracted from different voltage sweep range. **d** Band diagram before and after positive voltage sweep. The upper blue curve shows the conduction band before voltage sweep, and the dashed red curves indicate the reduced SBH at right contact and increased SBH at left contact. **e** Qualitative device model after positive voltage sweep. The size of the Schottky diode symbols refer to the different SBH at contacts. The bottom schematic shows the expected  $I$ - $V$  curves with small voltage range at forward diode state. **f** Band diagram before and after negative voltage sweep. The upper red curve shows the conduction band before voltage sweep, and the dashed blue curves indicate the reduced SBH at left contact and increased SBH at right contact. **g** Qualitative device model after negative voltage sweep. The bottom schematic shows the expected  $I$ - $V$  curves at small voltage range at backward diode state.

implies that the sulfur vacancies could be induced during the electrical measurement instead of EBI or other device fabrication process. In addition, electron dispersive X-ray spectroscopy line scan is performed (see Supplementary Fig. 9), indicating a non-van der Waals contact between metal and  $\text{ReS}_2$ , which is usually considered as the origin of FLP in 2D material contacts<sup>49,50</sup>. Moreover, temperature dependence measurement was carried out to extract the SBH at right contact under both FD state and BD state. Obvious right contact SBH reduction is found when the device was switched from BD state to FD state (see Supplementary Fig. 10). Evidently, it is confirmed that the RS is caused by voltage-bias-induced sulfur vacancies motion, which changes the SBH at contacts and further modulates the measured current.

With the confirmation of RS mechanism, we further investigate the rectification-mediated switching characteristics through different DC sweep schemes. As shown in Fig. 4a, it is worth noting that a positive voltage sweep changes the devices from BD state to FD state (termed as B-F transition) and vice versa for a negative sweep (termed as F-B transition). In addition, a small positive

voltage is always used to read the current and resistance value of both BD and FD states. Figure 4b and c shows an example on how a DC voltage sweep modulates the current level in the device. First, a consecutive five positive voltage sweeps ( $0 \rightarrow +5 \rightarrow 0$  V) is applied to the device, as shown in Fig. 4b. The measured current is shown to increase monotonously with the measurement cycle number. This is because the SBH at right contact is reduced during the cyclical sweep with positive bias. We then extract the current value at the first  $+0.5$  V in each cycle, as plotted in Fig. 4d. After a consecutive five positive cycles, we proceed to measure with another five negative sweep cycles immediately ( $0 \rightarrow -5 \rightarrow 0$  V), as shown in Fig. 4c. The negative voltage sweep changes the device from FD to BD state and the current is read at a small positive bias of  $+0.5$  V. We note that the current increases because the SBH at left contact is decreasing. In contrast, the SBH at the right contact is increased under negative sweep, which causes the current to decrease when it is read at the same positive bias of  $+0.5$  V.



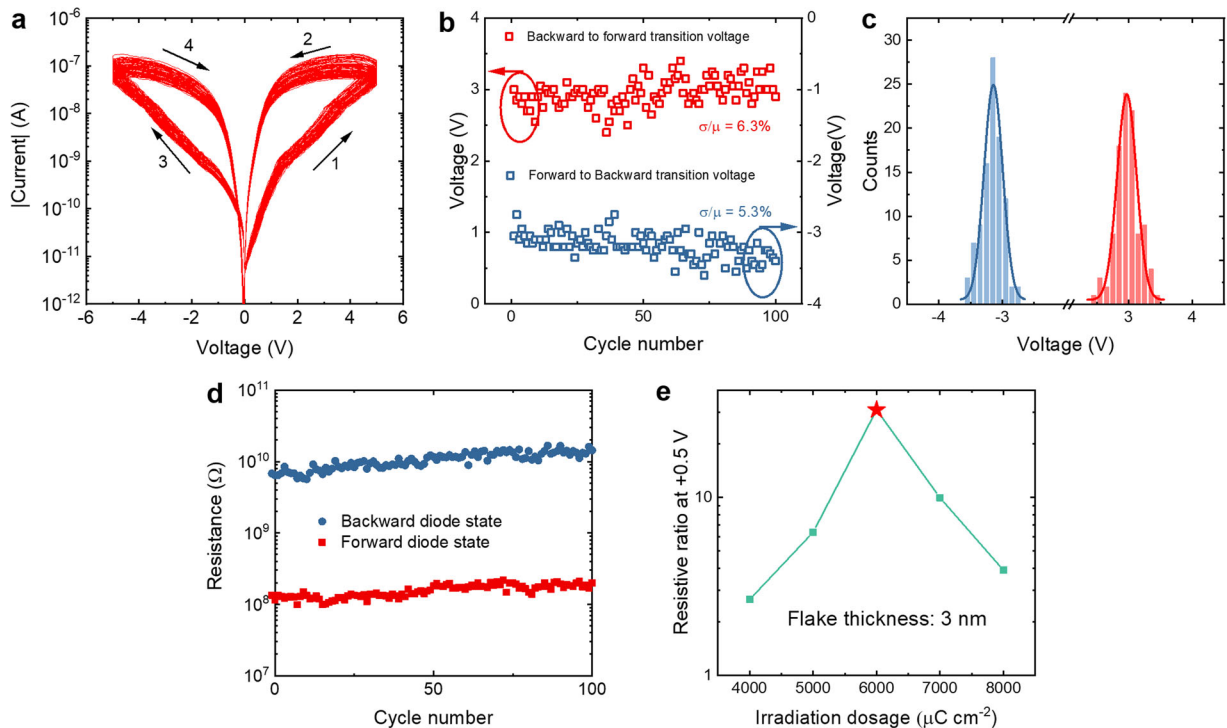
**Fig. 4** DC characteristics of  $\text{ReS}_2$  memristors. **a** Schematic of  $I$ - $V$  curve in linear scale. The black curved arrow in positive regime refers to the transition from backward diode state to forward diode state, and the black curved arrow in negative regime means the transition from forward diode state to backward diode state. **b**  $I$ - $V$  curves of five consecutive positive voltage sweeps ( $0 \rightarrow +5 \rightarrow 0$  V). Current increases with the sweep cycle number. **c**  $I$ - $V$  curves of another five cycles of sweep ( $0 \rightarrow -5 \rightarrow 0$  V). Current increases in negative regime and decreases in positive regime. **d** DC-programmed potentiation and depression. The red dots are extracted from the first  $+0.5$  V in different cycle sweep in **b** and blue dots are extracted at  $+0.5$  V in different cycle sweep in **c**. Insets are schematics showing the extraction of current values at the same base voltage of  $+0.5$  V. **e**  $I$ - $V$  curves measured under different voltage sweep ranges. The curves shown here are not measured consecutively. **f** Extracted current value at  $+0.5$  V under different sweep ranges. Inset shows that the calculated RS ratio increases with voltage sweep range.

Figure 4d shows the current values at  $+0.5$  V as extracted from the cyclical measurement. A clear increasing and decreasing current trend is observed by applying positive and negative voltage sweeps, respectively. Such DC-programmed synaptic potentiation and depression indicates the potential to use such devices for pulse-programmed synaptic behavior emulation. In addition, we compare the  $I$ - $V$  curves measured under different voltage sweep ranges as shown in Fig. 4e. At each sweep range, the device is measured for several cycles, and the stabilized  $I$ - $V$  curves are shown in this Figure. It is evident that the current is predominantly affected by the voltage sweep range. Figure 4f shows the current of FD state and BD state as extracted at  $+0.5$  V. Apparently, larger sweep range enlarges the difference between FD state and BD state. The calculated RS ratio is shown in the inset of Fig. 4f, which increases from around 20 times to 70 times as the sweep range is increased, manifesting its ability to achieve pulse amplitude-dependent synaptic plasticity.

For memristive devices, the RS  $I$ - $V$  curves under voltage sweep condition is important and should have the following characteristics: (i) large RS ratio between high resistance state (HRS) and low resistance state (LRS)<sup>24,28</sup>, (ii) small temporal variation of set voltage ( $V_{\text{set}}$ )<sup>18,51</sup>, and (iii) a stable endurance performance of HRS and LRS<sup>52</sup>. Figure 5a shows a typical forming-free gradual RS  $I$ - $V$  curve of an as-fabricated memristor that underwent an irradiation at  $6000 \mu\text{C cm}^{-2}$ . As opposed to other filamentary-based memristors which usually show an abrupt RS curves<sup>28,53</sup>, our device shows an electroforming-free gradual conductance change during voltage sweep, which manifests a non-filamentary RS mechanism. Additionally, the device as shown in Fig. 5a is measured for 100 DC cycles to extract the temporal variation. Here, we extracted the B-F and F-B transition voltages based on the nonlinearity of the  $I$ - $V$

curves<sup>45</sup>, which is larger than 5 ( $I \sim V^k$  and  $k \geq 5$ ) as shown in Fig. 5b. Details of transition voltage extraction are described in Supplementary Fig. 11. The variation and histogram of B-F and F-B transition voltages are depicted in Fig. 5b and c, respectively. The major advantage of the  $\text{ReS}_2$ -based memristors is the high temporal switching uniformity as compared to other filamentary memristors. Minimal temporal variations in B-F and F-B transition voltages of 6.3% and 5.3% are achieved, respectively, which is substantially lower than the filamentary memristors, and comparable with the improvements made in devices based on metal doping or ion transport confinement (see Supplementary Table 2)<sup>51,54,55</sup>. In addition, such low voltage variation is important for neuromorphic computing application to improve the learning accuracy<sup>31,56</sup>.

To investigate the endurance performance, the resistance values of FD state and BD state are extracted at  $0.5$  V and shown in Fig. 5d. A RS ratio of about 50 times is demonstrated. The increase in both FD state and BD state during endurance is due to device degradation during measurements. Like other memristors based on the rearrangement of atoms in switching layer<sup>57</sup>, such sulfur vacancy motion may induce damages in flakes, which leads to device degradation. The influence of EBI dosage and  $\text{ReS}_2$  thickness on the switching performance are investigated next. Figure 5e shows the average RS ratio of devices with a thickness of  $3$  nm with different EBI dosages, indicating that  $6000 \mu\text{C cm}^{-2}$  is the optimal irradiation dosage. The  $I$ - $V$  curves of memristors that are treated with different dosage within the same flake are shown in Supplementary Fig. 12, where  $6000 \mu\text{C cm}^{-2}$  condition still achieves the largest RS ratio. This is because a small dosage results in the least sulfur vacancies to trigger the RS behaviors. On the contrary, an excessively large dosage would severely increase the



**Fig. 5** Electrical characterization of ReS<sub>2</sub> memristor. **a** One-hundred cycles of  $I$ - $V$  sweep measurement. The black arrows show the voltage sweep order. **b** Extracted B-F and F-B transition voltages during the 100 DC sweep cycles. The voltage variation is calculated by the ratio of standard deviation ( $\sigma$ ) to average ( $\mu$ ). **c** Histogram of the extracted B-F and F-B transition voltages, both the distributions follow Gaussian distribution. **d** Resistance values as extracted at +0.5 V during 100 DC sweep cycles. The RS ratio is around 50 times. **e** The average RS ratio of 3-nm-thick flakes under different EBI dosages. Points from left to right were taken the average of 3, 3, 7, 5, 3 devices, respectively.

ReS<sub>2</sub> series resistance, resulting in the total resistance dominated by the ReS<sub>2</sub> series resistance instead of contact SBH, which leads to a smaller RS ratio. A plot of RS ratio of all devices with 6000 μC cm<sup>-2</sup> dosage is shown in Supplementary Fig. 13, where a critical thickness of 5 nm was found to achieve a tenfold increase in RS ratio. Beyond this thickness, RS behaviors are absent because thicker flakes have lower sulfur vacancy density under the same EBI dosage to trigger switching. It should be noted that the comparison of spatial (device-to-device) variation between devices is impractical. This is because our devices are fabricated by mechanical exfoliation, which renders it difficult to control the thickness, size, and shape of each flake that can influence the RS performance. However, further advances in CVD that produces large area and uniform growth of ReS<sub>2</sub> film would allow spatial variation in such devices to be investigated in future work.

#### Pulse measurement and application as artificial synapses

Emulation of biological synapse behaviors is implemented using our as-fabricated memristors. For an artificial synapse, our device operates similarly as compared to human nervous system. In human synapse, when a spike input arrives at the pre-synaptic neuron, ionic neurotransmitters will be released from pre-synaptic neuron, which triggers another spike in post-synaptic neuron. Similarly, in ReS<sub>2</sub>-based memristors, left and right electrodes are regarded as pre-synaptic and post-synaptic neurons, respectively. Sulfur vacancies, which mimic the neurotransmitters in biological synapse, are drifted by pulses to modulate the SBH at contacts. Figure 6a shows the programmed pulse waveform for modulating the synaptic weight of the device, which is extracted based on a base voltage of +0.5 V.

As it takes time for sulfur vacancies to diffuse back to their initial position, such alleviated FLP can be maintained when the next pulse arrives, which results in long-term synaptic plasticity. During the following measurement, voltage input is introduced through

left electrode, and the current is recorded as post-synaptic current (PSC). Figure 6b shows an example of the potentiation measurement in such devices. When positive pulses are applied, both measured currents at +5 V and +0.5 V are increased together, which is consistent with the DC potentiation in Fig. 4b. However, when negative pulses are applied (see Fig. 6c), the absolute current value at -5 V increases but the current measured at the same base voltage of +0.5 V decreases, which is consistent with the DC depression as shown in Fig. 4c. LTP and LTD are demonstrated and shown in Fig. 6d. A consecutive positive voltage pulse train in conjunction with another negative voltage pulse train is applied to the device, and the PSC as read at +0.5 V gradually increases or decreases during the positive pulses or negative pulses, respectively. Notably, at the beginning of positive and negative pulse train, the PSC response can be fitted by linear function, which is appropriate for neuromorphic computing<sup>58,59</sup>. Then, dynamic response of such artificial synapses is investigated by pulse voltage stress measurement with different pulse amplitudes (see Fig. 6e and f). In Fig. 6f, to achieve the same starting current, a pulse train with an amplitude of +3.5 V is applied before the negative pulse measurement. Similarly, the PSC as measured at +0.5 V increases during positive pulses and decreases with negative pulses.

Moreover, the dynamic response shows an amplitude dependence phenomenon. Device with larger positive pulse amplitude can achieve higher current and increase faster, and conductance stimulated by larger negative amplitude can be reduced more efficiently, implying the ability of such device in responding to different-amplitude stimulation, or SADP<sup>60</sup>. To further investigate the SADP behavior, synaptic weight change (change of current read at base voltage) with different pulse amplitudes is measured (see Fig. 6g). During the measurement, each point is extracted from the synaptic weight change between the first and tenth pulse. It is shown that larger pulse amplitude modulates the synaptic weight



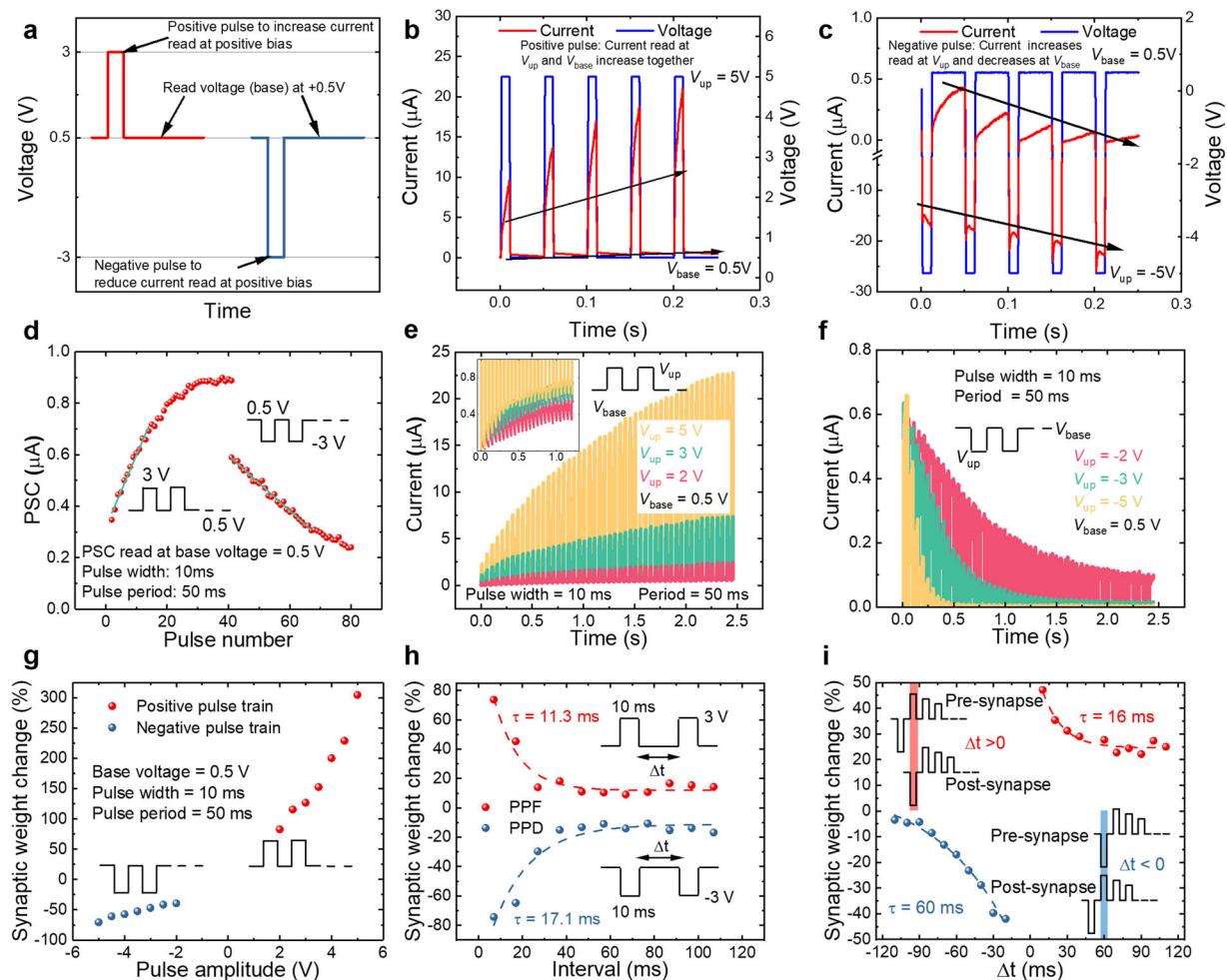


**Fig. 6 Pulse measurement for biological synapse emulation.** **a** Schematic of pulse waveform to modulate the synaptic weight. The synaptic weight refers to the current as read at +0.5V base voltage. **b** Potentiation measurement. Current read at +5V and +0.5V increases together. **c** Depression measurement. Current read at -5V increases, but current read at +0.5V decreases. **d** LTP and LTD measured by successive positive and negative pulses. The green lines show the linear fitting. PSC are measured at 0.5V base voltage. **e** Dynamic response of potentiation at pulse trains with amplitude of 2V, 3V, and 5V. Inset shows the base current read at 0.5V. **f** Dynamic response of depression at pulse trains with amplitude of -2V, -3V, and -5V. The currents shown in the figure were read at a base voltage of 0.5V. **g** SADP characteristic. Ten successive pulses were supplied to the device. Current before and after the pulse train were extracted to calculate the synaptic weight change. All parameters except amplitude were kept the same. **h** PPF and PPD measurements. Only two pulses were introduced to the device. The dashed lines are exponential fitting of the data. **i** STDP measurement. The dashed lines are exponential fitting. The insets show the schematic illustration of the equivalent pulse waveform design.

more effectively, which is consistent with the DC voltage sweep range dependence in Fig. 4f. In biological synapses, when spike-frequency adaptation happens in pre-synaptic neuron<sup>61</sup>, spikes will be generated with a variable frequency. In this way, the spike rate dependence of a synapse is also important and is analyzed in Fig. 6h. The data points are extracted from the synaptic weight change between the first and second pulse, so it is also regarded as PPF and PPD for positive and negative pulse condition, respectively. It is shown that smaller pulse interval (higher frequency) leads to larger synaptic weight change, because the device has less relaxation time during the shorter pulse interval<sup>2,25</sup>. Similar phenomenon is also found during dynamic response measurement with different pulse intervals, showing that pulse train with shorter interval needs less time to stimulate the synaptic weight to the same value (see Supplementary Fig. 14). STDP is also an important functionality for spiking neural networks<sup>3</sup>. Theoretically, STDP describes the synaptic weight change when both pre-synaptic and post-synaptic pulses are applied to a synapse with a certain time delay<sup>62</sup>. Usually, synaptic weight is increased with positive time delay, and decreased with negative time delay. Here, an equivalent designed pulse is

introduced into pre-synaptic neuron only to emulate the effect of both pulses, which are widely used in memristor synaptic applications<sup>3,25,63</sup>. The details of pulse waveform design are explained in Supplementary Fig. 15 and Supplementary Note 1. A typical STDP result is shown in Fig. 6i, showing the capability of this device to be applied to spiking neural networks with STDP learning rules<sup>62</sup>. By fitting the data with exponential function, the time constant of positive and negative delay are extracted to be 16ms and 60ms, respectively. Such microsecond response is analogous to human neurons<sup>64</sup>.

## DISCUSSION

In summary, electron-beam-irradiated  $\text{ReS}_2$ -based memristors with improved switching uniformity are demonstrated. The RS mechanism is attributed to the sulfur vacancies movement as induced by voltage bias, which causes SBH modulation at the contact regions. The formation of sulfur vacancies has been verified through material analysis. Moreover, forming-free RS behavior with minimal transition voltage variations of 6.3% and 5.3% are achieved under positive and



negative sweeps, respectively. In addition, a comprehensive demonstration of synaptic functionality is also implemented by such devices. The minimal temporal variation and successful emulation of synaptic plasticity in ReS<sub>2</sub>-based memristors hold great potential for deployment as artificial synapses in neuromorphic computing system.

## METHODS

### Device fabrication and characterization

First, few-layer ReS<sub>2</sub> flakes were exfoliated on heavily doped p-type silicon wafer with 90 nm silicon oxide. Next, Raman spectrum was carried out to align the crystal orientation ([1010]). Then, EBL was performed by electron beam lithography (EBL). After that, left/right electrodes were patterned by EBL again. In addition, a metal electrode layer of 10 nm Ti and 90 nm Au was deposited on the flakes by electron beam evaporator. Then the chip was put into acetone to proceed with standard lift-off process. Finally, the device was passivated by a PMMA layer.

DC sweeps were measured at room temperature in ambient condition using a probe station and an Agilent 4155B semiconductor analyzer. The Si substrate was grounded during all the *I*-*V* measurements. Pulse measurement was carried out by 4200-SCS Keithley semiconductor analyzer and a Cascade probe station. Low-temperature measurement was carried out by a Lakeshore CRX-VF cryogenic probe station at vacuum condition.

### Material characterization

ReS<sub>2</sub> samples with and without EBL were analyzed by AFM (Bruker Dimension Fastscan), Raman spectroscopy, PL spectroscopy (Witec Alpha 300R), XPS (Quantera PHI II), TEM, and STEM (Talos F200X). The excitation laser wavelength of Raman and PL spectroscopy was 532 nm. The laser power was below 100 μW to prevent additional damage to the flakes. For Raman spectroscopy, the peak positions were referenced to the silicon peak at 520 cm<sup>-1</sup>. XPS was collected by a monochromatic Al Kα X-ray source. The binding energies of all peaks were referenced to C 1s (285 eV).

## DATA AVAILABILITY

The data that support the plots within this article and other findings of this study are available from the corresponding author upon reasonable request.

Received: 11 July 2020; Accepted: 25 November 2020;

Published online: 04 January 2021

## REFERENCES

- Wang, Z. et al. Fully memristive neural networks for pattern classification with unsupervised learning. *Nat. Electron.* **1**, 137–145 (2018).
- Wang, Z. et al. Memristors with diffusive dynamics as synaptic emulators for neuromorphic computing. *Nat. Mater.* **16**, 101–108 (2017).
- Kuzum, D., Yu, S. & Philip Wong, H.-S. Synaptic electronics: materials, devices and applications. *Nanotechnology* **24**, 382001 (2013).
- Feng, X., Liu, X. & Ang, K.-W. 2D photonic memristor beyond graphene: progress and prospects. *Nanophotonics* **9**, 1579–1599 (2020).
- Wang, R. et al. Recent advances of volatile memristors: devices, mechanisms, and applications. *Adv. Intell. Syst.* **2**, 2000055 (2020).
- Li, Y. & Ang, K.-W. Hardware implementation of neuromorphic computing using large-scale memristor crossbar arrays. *Adv. Intell. Syst.* <https://doi.org/10.1002/aisy.202000137> (2020).
- Waser, R., Dittmann, R., Staikov, G. & Szot, K. Redox-based resistive switching memories – nanoionic mechanisms, prospects, and challenges. *Adv. Mater.* **21**, 2632–2663 (2009).
- Kim, S. et al. Experimental demonstration of a second-order memristor and its ability to biorealistically implement synaptic plasticity. *Nano Lett.* **15**, 2203–2211 (2015).
- Lee, M.-J. et al. A fast, high-endurance and scalable non-volatile memory device made from asymmetric Ta<sub>2</sub>O<sub>5-x</sub>/TaO<sub>2-x</sub> bilayer structures. *Nat. Mater.* **10**, 625–630 (2011).
- Park, G.-S. et al. In situ observation of filamentary conducting channels in an asymmetric Ta<sub>2</sub>O<sub>5-x</sub>/TaO<sub>2-x</sub> bilayer structure. *Nat. Commun.* **4**, 2382 (2013).
- Shibuya, K., Dittmann, R., Mi, S. & Waser, R. Impact of defect distribution on resistive switching characteristics of Sr<sub>2</sub>TiO<sub>4</sub> thin films. *Adv. Mater.* **22**, 411–414 (2010).
- Wong, H.-P. et al. Metal–Oxide RRAM. *Proc. IEEE* **100**, 1951–1970 (2012).

- Yang, J. J., Strukov, D. B. & Stewart, D. R. Memristive devices for computing. *Nat. Nanotechnol.* **8**, 13–24 (2013).
- Kim, K.-H. et al. A functional hybrid memristor crossbar-array/CMOS system for data storage and neuromorphic applications. *Nano Lett.* **12**, 389–395 (2012).
- Yang, Y. et al. Observation of conducting filament growth in nanoscale resistive memories. *Nat. Commun.* **3**, 1–8 (2012).
- Yang, Y. et al. Electrochemical dynamics of nanoscale metallic inclusions in dielectrics. *Nat. Commun.* **5**, 1–9 (2014).
- Waser, R. & Aono, M. Nanoionics-based resistive switching memories. *Nat. Mater.* **6**, 833–840 (2007).
- Choi, S. et al. SiGe epitaxial memory for neuromorphic computing with reproducible high performance based on engineered dislocations. *Nat. Mater.* **17**, 335–340 (2018).
- Akinwande, D. et al. Graphene and two-dimensional materials for silicon technology. *Nature* **573**, 507–518 (2019).
- Jurca, T. et al. Low-temperature atomic layer deposition of MoS<sub>2</sub> films. *Angew. Chem. Int. Ed.* **56**, 4991–4995 (2017).
- Cui, F. et al. Tellurium-assisted epitaxial growth of large-area, highly crystalline ReS<sub>2</sub> atomic layers on mica substrate. *Adv. Mater.* **28**, 5019–5024 (2016).
- Gao, L. et al. Face-to-face transfer of wafer-scale graphene films. *Nature* **505**, 190–194 (2014).
- Kang, K. et al. Layer-by-layer assembly of two-dimensional materials into wafer-scale heterostructures. *Nature* **550**, 229–233 (2017).
- Feng, X. et al. A fully printed flexible MoS<sub>2</sub> memristive artificial synapse with femtojoule switching energy. *Adv. Electron. Mater.* **5**, 1900740 (2019).
- Shi, Y. et al. Electronic synapses made of layered two-dimensional materials. *Nat. Electron.* **1**, 458–465 (2018).
- Ge, R. et al. Atomistor: nonvolatile resistance switching in atomic sheets of transition metal dichalcogenides. *Nano Lett.* **18**, 434–441 (2018).
- Xu, R. et al. Vertical MoS<sub>2</sub> double layer memristor with electrochemical metallization as an atomic-scale synapse with switching thresholds approaching 100 mV. *Nano Lett.* **19**, 2411–2417 (2019).
- Bessonov, A. A. et al. Layered memristive and memcapacitive switches for printable electronics. *Nat. Mater.* **14**, 199–204 (2015).
- Huh, W. et al. Synaptic barristor based on phase-engineered 2D heterostructures. *Adv. Mater.* **30**, 1801447 (2018).
- Pi, S. et al. Memristor crossbar arrays with 6-nm half-pitch and 2-nm critical dimension. *Nat. Nanotechnol.* **14**, 35–39 (2019).
- Xia, Q. & Yang, J. J. Memristive crossbar arrays for brain-inspired computing. *Nat. Mater.* **18**, 309–323 (2019).
- Li, D. et al. MoS<sub>2</sub> memristors exhibiting variable switching characteristics toward biorealistic synaptic emulation. *ACS Nano* **12**, 9240–9252 (2018).
- Zhu, X., Li, D., Liang, X. & Lu, W. D. Ionic modulation and ionic coupling effects in MoS<sub>2</sub> devices for neuromorphic computing. *Nat. Mater.* **18**, 141–148 (2019).
- Sangwan, V. K. et al. Multi-terminal memtransistors from polycrystalline monolayer molybdenum disulfide. *Nature* **554**, 500–504 (2018).
- Wang, L. et al. Artificial synapses based on multiterminal memtransistors for neuromorphic application. *Adv. Funct. Mater.* **29**, 1901106 (2019).
- Tongay, S. et al. Monolayer behaviour in bulk ReS<sub>2</sub> due to electronic and vibrational decoupling. *Nat. Commun.* **5**, 3252 (2014).
- Shim, J. et al. High-performance 2D rhenium disulfide (ReS<sub>2</sub>) transistors and photodetectors by oxygen plasma treatment. *Adv. Mater.* **28**, 6985–6992 (2016).
- Horzum, S. et al. Formation and stability of point defects in monolayer rhenium disulfide. *Phys. Rev. B* **89**, 155433 (2014).
- He, Q. et al. Deeply exploring anisotropic evolution toward large-scale growth of monolayer ReS<sub>2</sub>. *ACS Appl. Mater. Interfaces* **12**, 2862–2870 (2020).
- Lin, Y.-C. et al. Single-layer ReS<sub>2</sub>: two-dimensional semiconductor with tunable in-plane anisotropy. *ACS Nano* **9**, 11249–11257 (2015).
- Xu, K., Cao, P. & Heath, J. R. Scanning tunneling microscopy characterization of the electrical properties of wrinkles in exfoliated graphene monolayers. *Nano Lett.* **9**, 4446–4451 (2009).
- Chenet, D. A. et al. In-plane anisotropy in mono- and few-layer ReS<sub>2</sub> probed by Raman spectroscopy and scanning transmission electron microscopy. *Nano Lett.* **15**, 5667–5672 (2015).
- Huang, W. et al. Ion beam defect engineering on ReS<sub>2</sub>/Si photocathode with significantly enhanced hydrogen evolution reaction. *Adv. Mater. Interfaces* **6**, 1801663 (2019).
- McDonnell, S., Addou, R., Buie, C., Wallace, R. M. & Hinkle, C. L. Defect-dominated doping and contact resistance in MoS<sub>2</sub>. *ACS Nano* **8**, 2880–2888 (2014).
- Jadwiszczak, J. et al. MoS<sub>2</sub> memtransistors fabricated by localized helium ion beam irradiation. *ACS Nano* **13**, 14262–14273 (2019).
- Song, S. H., Joo, M.-K., Neumann, M., Kim, H. & Lee, Y. H. Probing defect dynamics in monolayer MoS<sub>2</sub> via noise nanospectroscopy. *Nat. Commun.* **8**, 2121 (2017).
- Noh, J.-Y., Kim, H. & Kim, Y.-S. Stability and electronic structures of native defects in single-layer MoS<sub>2</sub>. *Phys. Rev. B* **89**, 205417 (2014).

48. Osvald, J. Back-to-back connected asymmetric Schottky diodes with series resistance as a single diode. *Phys. Status Solidi A* **212**, 2754–2758 (2015).
49. Liu, Y. et al. Approaching the Schottky–Mott limit in van der Waals metal–semiconductor junctions. *Nature* **557**, 696–700 (2018).
50. Schulman, D. S., Arnold, A. J. & Das, S. Contact engineering for 2D materials and devices. *Chem. Soc. Rev.* **47**, 3037–3058 (2018).
51. Liu, Q. et al. Improvement of resistive switching properties in  $ZrO_2$ -based ReRAM with implanted metal ions. In *2009 Proc. European Solid State Device Research Conference (IEEE, Athens, Greece, 2009)*.
52. Lanza, M. et al. Recommended methods to study resistive switching devices. *Adv. Electron. Mater.* **5**, 1800143 (2019).
53. Wei, Z. et al. Highly reliable TaOx ReRAM and direct evidence of redox reaction mechanism. In *2008 IEEE International Electron Devices Meeting (IEEE, San Francisco, CA, USA, 2008)*.
54. Yoon, J. H. et al. Highly improved uniformity in the resistive switching parameters of  $TiO_2$  thin films by inserting Ru nanodots. *Adv. Mater.* **25**, 1987–1992 (2013).
55. Chang, W.-Y., Lin, C.-A., He, J.-H. & Wu, T.-B. Resistive switching behaviors of ZnO nanorod layers. *Appl. Phys. Lett.* **96**, 242109 (2010).
56. Zidan, M. A., Strachan, J. P. & Lu, W. D. The future of electronics based on memristive systems. *Nat. Electron.* **1**, 22–29 (2018).
57. Wang, Z. et al. Resistive switching materials for information processing. *Nat. Rev. Mater.* **5**, 173–195 (2020).
58. Chen, P. -Y., Peng, X. & Yu, S. NeuroSim+: an integrated device-to-algorithm framework for benchmarking synaptic devices and array architectures. In *2017 IEEE International Electron Devices Meeting (IEDM) (IEEE, San Francisco, CA, USA, 2017)*.
59. Yu, S. Neuro-inspired computing with emerging nonvolatile memories. *Proc. IEEE* **106**, 260–285 (2018).
60. Chen, L. et al. A van der Waals synaptic transistor based on ferroelectric  $Hf_{0.5}Zr_{0.5}O_2$  and 2D tungsten disulfide. *Adv. Electron. Mater.* **6**, 2000057 (2020).
61. Benda, J. & Herz, A. V. M. A universal model for spike-frequency adaptation. *Neural Comput.* **15**, 2523–2564 (2003).
62. Bi, G. & Poo, M. Synaptic modifications in cultured hippocampal neurons: dependence on spike timing, synaptic strength, and postsynaptic cell type. *J. Neurosci.* **18**, 10464–10472 (1998).
63. Wu, Y. et al. AlOx-based resistive switching device with gradual resistance modulation for neuromorphic device application. In *2012 4th IEEE International Memory Workshop (IEEE, Milan, Italy, 2012)*.
64. Song, S., Miller, K. D. & Abbott, L. F. Competitive Hebbian learning through spike-timing-dependent synaptic plasticity. *Nat. Neurosci.* **3**, 919–926 (2000).

## ACKNOWLEDGEMENTS

This research is supported by A\*STAR Science and Engineering Research Council (No. A2083c0061), and National Research Foundation, Singapore (NRF-CRP22-2019-0007). S.L. and B.L. contributed equally to this work. We thank X. Gong in the Department of

Electrical and Computer Engineering, National University of Singapore, for valuable help in device measurements.

## AUTHOR CONTRIBUTIONS

This project was supervised and directed by K.-W.A. S.L. and K.-W.A. conceived and designed the experiments. S.L. and B.L. contributed equally. S.L. performed the device fabrication. S.L. and B.L. conducted the electrical measurements. L.C. performed the material characterization. All authors contributed to the discussion and results analysis. S.L. and K.-W.A. wrote the manuscript.

## COMPETING INTERESTS

The authors declare no competing interests.

## ADDITIONAL INFORMATION

**Supplementary information** is available for this paper at <https://doi.org/10.1038/s41699-020-00190-0>.

**Correspondence** and requests for materials should be addressed to X.F. or K.-W.A.

**Reprints and permission information** is available at <http://www.nature.com/reprints>

**Publisher's note** Springer Nature remains neutral with regard to jurisdictional claims in published maps and institutional affiliations.



**Open Access** This article is licensed under a Creative Commons Attribution 4.0 International License, which permits use, sharing, adaptation, distribution and reproduction in any medium or format, as long as you give appropriate credit to the original author(s) and the source, provide a link to the Creative Commons license, and indicate if changes were made. The images or other third party material in this article are included in the article's Creative Commons license, unless indicated otherwise in a credit line to the material. If material is not included in the article's Creative Commons license and your intended use is not permitted by statutory regulation or exceeds the permitted use, you will need to obtain permission directly from the copyright holder. To view a copy of this license, visit <http://creativecommons.org/licenses/by/4.0/>.

© The Author(s) 2021